Available online at www.sciencedirect.com
ScienceDirect
Acta Materialia 57 (2009) 6090–6101
Acta MATERIALIA
www.elsevier.com/locate/actamat

Fundamental differences in the plasticity of periodically twinned nanowires in Au, Ag, Al, Cu, Pb and Ni

C. Deng, F. Sansoz *

School of Engineering and Materials Science Program, The University of Vermont, Burlington, VT 05405, USA

Received 18 May 2009; received in revised form 6 July 2009; accepted 14 August 2009
Available online 15 September 2009

Abstract

The role played by nanoscale twins is becoming increasingly important in order to understand plasticity in nanowires synthesized from metals. In this paper, molecular dynamics simulations were performed to investigate the synergistic effects of stacking fault energy and twin boundary on the plasticity of a periodically twinned face-centered cubic (fcc) metal nanowire subjected to tensile deformation. Circular nanowires containing parallel (1 1 1) coherent twin boundaries (CTBs) with constant twin boundary spacing were simulated in Au, Ag, Al, Cu, Pb and Ni using different embedded-atom-method interatomic potentials. The simulations revealed a fundamental transition of plasticity in twinned metal nanowires from sharp yield and strain-softening to significant strain-hardening as the stacking fault energy of the metal decreases. This effect is shown to result from the relative change, as a function of the unstable stacking fault energy, between the stress required to nucleate new dislocations from the free surface and that to overcome the resistance of CTBs to the glide of partial dislocations. The relevance of our predictions to realistic nanowires in terms of microstructure, geometry and accuracy in predicting the generalized planar and stacking fault energy curves is also addressed. Our findings show clear evidence that the plastic flow of twinned nanowires under tension differs markedly between fcc metals, which may reconcile some conflicting observations made in the past.

Keywords: Plastic deformation; Grain boundary twin; Nanostructure; Molecular dynamics; Simulation

1. Introduction

The plasticity of face-centered cubic (fcc) metal wires and pillars with submicron or nanoscale diameters has drawn considerable interest, and has been extensively studied in recent years by nanomechanical experiments [1–10] and molecular dynamics (MD) simulations [11–20]. Most observations have proved that fcc metals in nanosized volumes possess much higher strength than that of their bulk counterparts. To date, however, some aspects of the plasticity of metal nanowires (NWs) remain elusive, primarily on two accounts as follows.

First, there are some apparent contradictions about the modes of plastic deformation of metal NWs between experimental observations and atomistic predictions. Large size-dependent strengthening effects have been found in 200-nm-diameter Al NWs under tension [9] and 160-nm-diameter [1 1 1]-oriented Ni pillars under compression from in situ transmission electron microscopy (TEM) experiments [6]. It was observed that dislocations could easily escape at the free surface due to the large surface-to-volume ratio in such small samples. These observations have led to suggest that dislocation nucleation is source-limited in small deformed volumes, which increases the stress to nucleate new dislocations as further deformation is applied. Other experimental studies [2,4,5,8] have also revealed that fcc metal NWs and nanopillars exhibit pronounced strain-hardening after plastic yielding, although the mechanism responsible for this effect is still under active debate. Using atomic force microscopy-based bending experiments, Wu et al. [1] have also measured significant strain-hardening in Au NWs with diameters down to 40 nm, but these authors suggested a different mechanism

* Corresponding author.
E-mail address: frederic.sansoz@uvm.edu (F. Sansoz).

1359-6454/$36.00
doi:10.1016/j.actamat.2009.08.035

by which interactions between dislocations and grain boundaries, similar to the hardening mechanisms observed in bulk metals [21], may still operate at this scale.

In stark contrast, the plastic deformation of metal NWs studied by MD simulations [11–20] has shown either limited or no strain-hardening at all. For example, the stress–strain curves of Au NWs predicted from MD simulations [11–16] all indicated a sharp yield point followed by severe strain-softening, while the yield stress was found to be much higher than that in bulk gold, similar to the mechanical behavior of defect-free Au whiskers from classic experiments by Brenner [22]. This whisker-like behavior has also been predicted in the deformation of different single-crystalline metal NWs, such as Cu [17,18], Al [19] and Ni [20]. However, it was also found by MD simulations that general grain boundaries would lower the yield strength and increase the ductility of Ni NWs subjected to tensile deformation [23]. It is therefore not clear why microstructure effects predicted by simulation differ from those observed experimentally.

It was argued by Maaβ et al. [24] that the occurrence of internal microstructures and their potential effects on plasticity in nanosized metals may account for the observed discrepancy between simulation and experiment. By studying the initial microstructure of undeformed metal nanopillars fabricated by micromachining techniques from a bulk single crystal as in Refs. [2,4,5,8], these authors have shown that several microstructural defects, such as misorientations at the pillar base, grain boundaries, strain gradients and twin defects in the pillar body, were present, which may have contributed to strong hardening effects. Similarly, the TEM images of Au NWs tested by Wu et al. [1] also showed a distribution of parallel coherent twin boundaries (CTBs) along the NW axis, similar to a bamboo-like structure. Therefore, the plastic behavior of metal NWs can only be fully understood if one gains fundamental insights into the process of nucleation and propagation of dislocations from free surfaces and their interactions with pre-existing defects.

Second, large attention has already been paid to the role of CTBs in the plasticity of fcc metals, as a special type of grain boundary commonly formed during synthesis in various nanomaterials [3,25,26]. However, important differences have been reported in earlier atomistic studies [13,27–31] about the influence of microstructure on plasticity in fcc metal NWs with nanoscale twins. In Au NWs, for example, Hyde et al. [13] have found using MD simulations that the tensile yield stress is 18–22% less when one (1 1 1) twin boundary is added, as opposed to that in a perfect NW with corresponding diameter. On the contrary, Afanasyev and Sansoz [27] have observed significant strengthening in circular Au nanopillars by introducing several parallel (1 1 1) CTBs, which resulted from the formation of Lomer–Cottrell locks at the intersection of partial dislocations and CTBs. Moreover, Deng and Sansoz [28] have recently shown the existence of a transition in plasticity mechanism from whisker-like, strain-softening behavior to strain-hardening regime, as a function of the ratio of NW diameter over twin boundary spacing, in twinned Au NWs under tension.

In contrast, a different picture has emerged in the plasticity of Cu NWs with nanoscale twins. While strengthening effects caused by (1 1 1) CTBs were observed by Cao et al. [29] in Cu NWs with square cross-section, Zhang and Huang [30,31] clearly demonstrated that CTB-induced strengthening effects completely disappear in twinned Cu NWs when the sample shape changes from square cross-section to circular cross-section.

Furthermore, transmission of dislocations through CTBs has largely been studied by atomistic methods, revealing that CTBs exert a repulsive force against the lattice dislocations approaching them [32], and act as strong barriers to slip [33–37]. By investigating the interaction mechanisms of screw and non-screw dislocations with CTBs in different fcc metals, Jin et al. [38,39] have concluded that gliding dislocations may either dissociate on the CTB plane or cut through the CTB and propagate into the adjacent twin grain depending on the metal investigated, due to the material-dependent energy barriers to form partial dislocations at the twin–slip intersection. Based on Jin et al.'s findings, it is possible to deduce that the unstable stacking fault energy (γ_{USF}) and unstable twinning energy (γ_{UTF}) of the metal, which represents the energy barrier for the formation of Shockley partial dislocations and twin faults, respectively [40,41], may largely account for some of the differences in plasticity observed in twinned NWs of different metals, primarily due to the influence of γ_{USF} and γ_{UTF} on dislocation nucleation and dislocation–CTB interactions.

The aim of this work is to use MD simulations with different embedded-atom method (EAM) potentials to systematically study the effects of pre-existing periodic CTBs on the plastic flow of fcc metal NWs under tension, and their dependence on the generalized planar and stacking fault energy curves [42]. The paper is divided as follows. Section 2 presents the details of the computational procedure to simulate the tensile deformation of various fcc metal NWs and study the slip transmission through CTBs in corresponding bulk metals. Section 3 shows that some fundamental differences in tensile behavior exist between different twinned metal NWs, as a function of the EAM potential. In Section 4, we discuss the transition of plasticity and underlying mechanisms in fcc metal NWs due to the change of γ_{USF}. This section also presents the dependency of the stress for dislocation nucleation from free surfaces, and that to overcome the resistance of CTBs to the glide of partial dislocations, as a function of γ_{USF}, in different metals. The relevance of our predictions to realistic NWs in terms of microstructure, geometry and interatomic potential accuracy is also addressed.

2. Computational methods

2.1. Tensile deformation of twinned NWs

Non-equilibrium MD simulations were performed using LAMMPS [43] with ten EAM potentials developed for Au, Al, Ag, Cu, Pb and Ni [44–50]; see Table 1. The geometry

Table 1
Calculated unstable stacking fault energy (γ_{USF}), intrinsic stacking fault energy (γ_{SF}), unstable twinning fault energy (γ_{UTF}) and the stress for dislocation nucleation in twinned NW (σ_y), twin-free NW (σ_{SC}) and twin-free bulk metals (σ_{HN}), the maximum flow stress in twinned NWs (σ_m), and the maximum resistance imposed by CTBs to the glide of partial dislocations (σ_R) in fcc metals predicted from different EAM potentials. The experimental values of intrinsic stacking fault energy found in the literature γ_{SF} (exp.), and the occurrence of strain-hardening with corresponding yielding mechanism (see Section 4.1 for details) in each simulated NW are listed for comparison.

Metal	EAM potential	Energy (mJ m^{-2})				Mechanical behavior (GPa)					Strain-hardening effects	Yielding mechanism
		γ_{USF}	γ_{SF}	γ_{SF} (exp.)	γ_{UTF}	σ_y	σ_m	σ_{SC}	σ_R	σ_{HN}		
Au	Au_{GRS}[a]	92.0	41.6	32–46.4[a]	100.6	3.0	4.0	3.2	4.6	5.5	Yes	I
	Au_{u3}[b]	95.1	4.2		97.4	3.3	4.5	3.6	5.3	7.0	Yes	I
Ag	Ag_{VC}[c]	90.4	13.9	16[h]	97.8	4.9	4.9	4.8	4.7	6.1	No	II
	Ag_{u3}[b]	117.9	0.8		118.6	5.9	5.9	6.1	5.3	7.3	No	II
	Ag_{Cu}[d]	38.3	1.5		39.3	1.0	1.4	1.0	1.7	2.0	Yes	I
Cu	Cu_{Ag}[d]	60.0	7.6	45[i]	63.0	1.9	2.4	2.1	3.0	3.8	Yes	I
	Cu_{Mishin}[e]	161.0	43.5		182.4	9.4	9.4	9.4	8.8	11.5	No	II
Al	Al[f]	166.7	144.8	120–144[j]	219.2	4.2	4.2	4.4	3.5	5.3	No	III
Pb	Pb[g]	56.3	0.0	6–10[l]	56.4	0.6	1.1	0.6	1.3	2.0	Yes	I
Ni	Ni[f]	365.5	123.6	125[k]	425.4	22.3	22.3	21.7	16.6	23.4	No	II

[a] [44].
[b] [45].
[c] [46].
[d] The potential is for Ag–Cu alloy [47].
[e] [48].
[f] [49].
[g] The potential is for Pb–Cu alloy [50].
[h] [52].
[i] [53].
[j] [54,55].
[k] [56].
[l] [57].

of a [1 1 1]-oriented NW with a circular cross-section containing periodically distributed (1 1 1) CTBs was simulated by atomistic method as shown in Fig. 1. Periodic boundary conditions were imposed along the [1 1 1] axis, while the NW was kept free in all other directions. For all simulations, NW diameter, NW periodic length along the axis and twin boundary spacing were kept equal to 30a, 80a and 10a, respectively, where a is the lattice constant. The models consisted of ~240,000 atoms. The timestep was

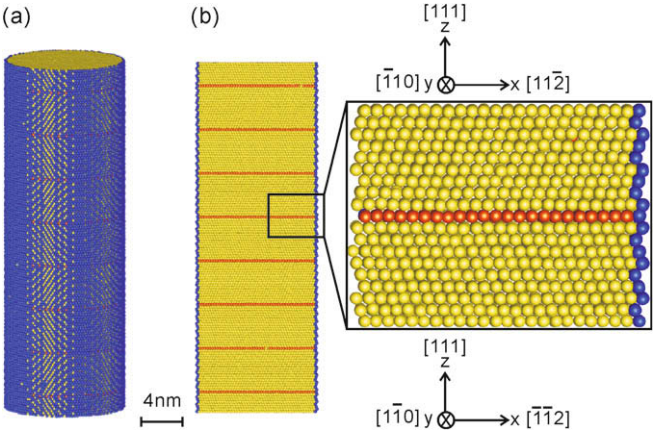

Fig. 1. Atomistic model of circular nanowire with (1 1 1) coherent twin boundaries in fcc metals. (a) Full atomistic view. (b) Close-up view of the coherent twin boundary. Atom colors correspond to the crystal structure according to Ackland and Jones' analysis.

5 fs. Each model was relaxed prior to deformation for 20,000 steps (100 ps) under zero pressure (using constant NPT integration with Nose–Hoover thermostat). The NW was deformed in tension by straining the simulation box at a constant strain rate of 5×10^7 s^{-1} along the [1 1 1] direction with NVT integration at 300 K. Ackland and Jones' analysis [51] was used to visualize the atomic structures during deformation. The tensile deformation of NWs with no CTBs was also simulated for comparison.

Furthermore, we simulated the tensile deformation of a twinned Ag NW with a square cross-section (~300,000 atoms) in order to characterize the influence of geometry on dislocation nucleation, as studied in Refs. [30,31]. The side of the square cross-section was 30a. All other conditions were identical to those for the circular NWs.

2.2. Simulation of twin–slip interactions in fcc bulk metals

The resistance encountered by Shockley partial dislocations moving towards a CTB was studied by deforming a twinned cubic model of size 40a (~270,000 atoms) with two pre-introduced $1/6(1\,1\,\bar{1})\langle 1\,1\,2\rangle$ partial dislocations inside (see Fig. 2). Periodic boundaries were imposed to all three axes, so no free surface is considered in this model. The twin boundary spacing was equal to 20a. Tensile deformation was simulated by stretching the simulation box along the [1 1 1] direction at a constant strain rate of 5×10^7 s^{-1},

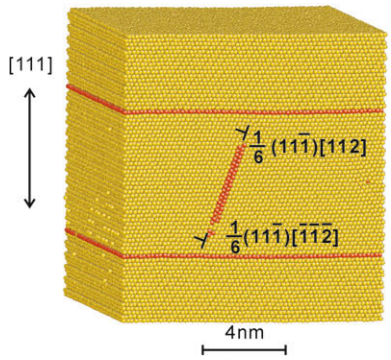

Fig. 2. Atomistic model with three-dimensional periodicity for analysis of maximum stress for the resistance of twin boundaries to the glide of partial dislocations in bulk fcc metals.

while imposing zero lateral pressure using constant NPT integration at 300 K. The maximum stress for the resistance of CTBs to dislocation glide was directly determined in this model at the stress causing the two partial dislocations to fully transmit through the CTBs from the parent grain to the twin grain. The stress–strain curves of fully periodic cubic models with no twins were also simulated under the same conditions to determine the stress for homogeneous nucleation of Shockley partials in each metal.

2.3. Calculation of generalized planar and stacking fault energy curves

Zimmerman et al. [42] have shown that the unstable stacking fault energy γ_{USF} corresponds to the potential energy for partial $\{1\,1\,1\}\langle 1\,1\,2\rangle$ slip in fcc metals with a Burgers vector b_p of magnitude $a/\sqrt{6}$. Here, the values of intrinsic stacking fault energy (γ_{SF}) and unstable stacking fault energy (γ_{USF}) were calculated for each EAM potential on an intrinsic stacking fault formed by rigidly shifting the upper half of a single-crystal cubic model along the $[1\,1\,\bar{2}]$ direction in a (1 1 1) plane, while fixing the lower half, as described in Ref. [48]. Similar to Ref. [41], the unstable twinning fault energy (γ_{UTF}) of each metal was calculated by rigidly shifting the single-crystal model along the $[1\,1\,\bar{2}]$ direction in a (1 1 1) plane that is one atom layer above a stacking fault previously formed by shearing. Only in-plane periodic boundary conditions were imposed in this case. The energy was calculated by subtracting the total energy of the simulation box prior to deformation from that in the deformed configuration. The predicted values of γ_{USF}, γ_{SF} and γ_{UTF} for different fcc metals along with several experimental values for γ_{SF} from the literature [44,52–57] are listed in Table 1.

3. Results

3.1. Tensile deformation of a circular Au NW with periodic CTBs

The tensile stress–strain curve of a twinned circular Au NW predicted from the GRS EAM potential (Au_{GRS}) [44] and corresponding stages of deformation are presented in Fig. 3. This figure shows that the deformation of Au NWs is characterized by three dominant regimes: elastic, strain-hardening and strain-softening regimes. It is worth noting that the initial yield stress ($\sigma_y = 3.0$ GPa) and the maximum flow stress ($\sigma_m = 4.0$ GPa) are markedly different in Au NWs due to the important linear strain-hardening effect. We found from the analysis of deformation mechanisms that the onset of plasticity corresponds to the emission of $\{1\,1\,1\}\langle 1\,1\,2\rangle$ leading partial dislocations from the free surface at the intersection with CTBs (Fig. 3a), which is consistent with the mechanism reported previously [27]. Fig. 3b also shows that each leading partial dislocation is blocked by a CTB after the initial yield, which increases the stress to nucleate new partial dislocations. Strain-hardening effects stop, i.e., the flow stress reaches σ_m, when in turn trailing partial dislocations are able to nucleate, as shown in the dashed frames in Fig. 3c. Here it is important to note that the strain-softening process beyond σ_m is accompanied by the transmission of dislocations through CTBs and, to some extent, their escape at the free surface as shown in Fig. 3c and d.

3.2. Tensile deformation of a circular Cu NW with periodic CTBs

Fig. 4 shows the tensile stress–strain curve and corresponding stages of deformation for a twinned Cu NW with a circular cross-section predicted from the Mishin EAM potential (Cu_{Mishin}) [48]. A key result is that this NW does not exhibit any strain-hardening, as opposed to the tensile behavior of Au NWs with corresponding twin boundary spacing. The onset of yielding in the Cu NW is also associated with the nucleation and propagation of $\{1\,1\,1\}\langle 1\,1\,2\rangle$ leading partials from the intersection between CTBs and the free surface (Fig. 4a). However, the partial dislocations nucleated from the free surface are able to cut through the CTB without being blocked, which causes a sharp yield and substantial stress drop immediately after the initial yield point (Fig. 4b). Therefore, under these conditions, both yield stress and maximum flow stress are identical ($\sigma_y = \sigma_m = 9.4$ GPa). Furthermore, Fig. 4c shows that dislocations have escaped at the free surface, as indicated by the significant surface deformation and decrease in the number of dislocations inside the NW, in comparison to Fig. 4b.

3.3. Tensile deformation of other types of fcc metal NW with periodic CTBs

The tensile stress–strain curves of twinned Au, Al, Ag, Cu, Ni and Pb NWs predicted from different EAM potentials are represented in Fig. 5 with stress values normalized by the Young's modulus E. Two distinctive sets of plastic behavior can be noted in Fig. 5 and Table 1. NWs simulated using Au_{U3}, Pb, Ag_{Cu} and Cu_{Ag} potentials show significant strain-hardening, similar to that observed in the

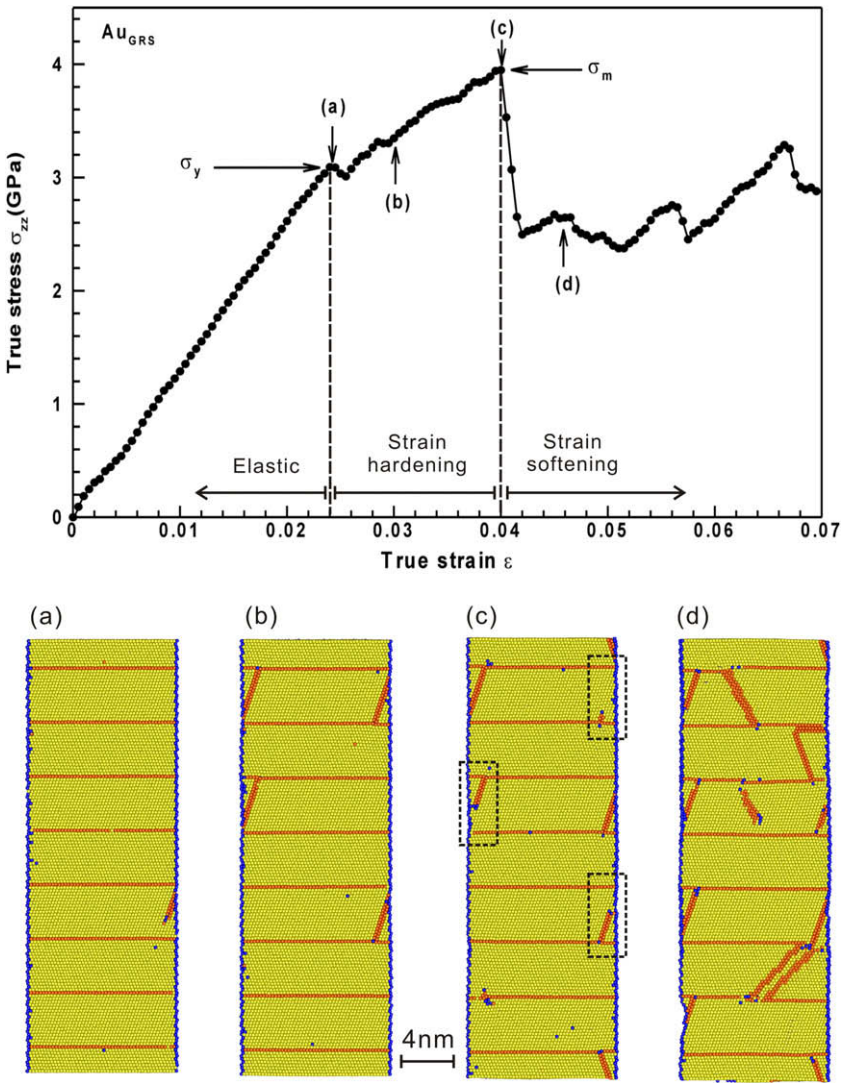

Fig. 3. Tensile stress–strain curve of a periodically twinned Au nanowire predicted from GRS EAM potential. Snapshots at different stages of deformation are shown from (a) to (d). (a) Nucleation of the very first dislocation at initial yield stress (σ_y). (b) Leading partial dislocations stopped by twin boundaries. Nanowire deformation (c) at and (d) after the maximum flow stress (σ_m). Atom colors correspond to the crystal structure. Dashed frames in (c) show the emission of trailing partial dislocations from the free surface.

Au_{GRS} NW. Moreover, the strain-hardening rate $d\sigma/d\varepsilon$ (normalized by E) calculated from Fig. 5 is almost constant (0.57 ± 0.07) in all strain-hardened NWs, which indicates that the hardening process in these NWs is related to the same mechanism. On the contrary, NWs simulated with the Ni, Al, Ag_{VC} and Ag_{u3} potentials show no strain-hardening, similar to the observations made in the Cu_{Mishin} NW presented above.

3.4. Yielding mechanisms in twinned fcc metal NWs as a function of EAM potential

The atomic-scale analysis of yielding mechanisms based on crystal structure [51] and local von Mises strain calculations [58,59] is shown in Fig. 6 for three EAM potentials. This figure confirms that the onset of plasticity in all fcc metal NWs is associated with the emission of $\{1\,1\,\bar{1}\}\langle 1\,1\,2\rangle$ partial dislocations from the free surface. However, three distinctive mechanisms of dislocation–CTB interaction, referred to as Mechanisms I–III in the following, can be observed in the NWs at the initial yield point, depending on the EAM potential.

In Mechanism I, it is observed that the glide of leading partial dislocations emitted from the surface is stopped immediately by the CTBs, as shown on the close-up view in Fig. 6a for the Au_{GRS} NW. Such yielding mechanism takes place in metal NWs simulated with Au_{GRS}, Au_{U3}, Pb, Ag_{Cu} and Cu_{Ag} potentials. As a result of the dislocation blockage, significant strain-hardening occurs in these NWs with further applied strain. The maximum flow stress σ_m is reached when secondary partial dislocations are able to emit from different defects on the free surface, such as twin boundaries or stacking faults left earlier by the leading partial dislocations emitted at the initial yield point. A

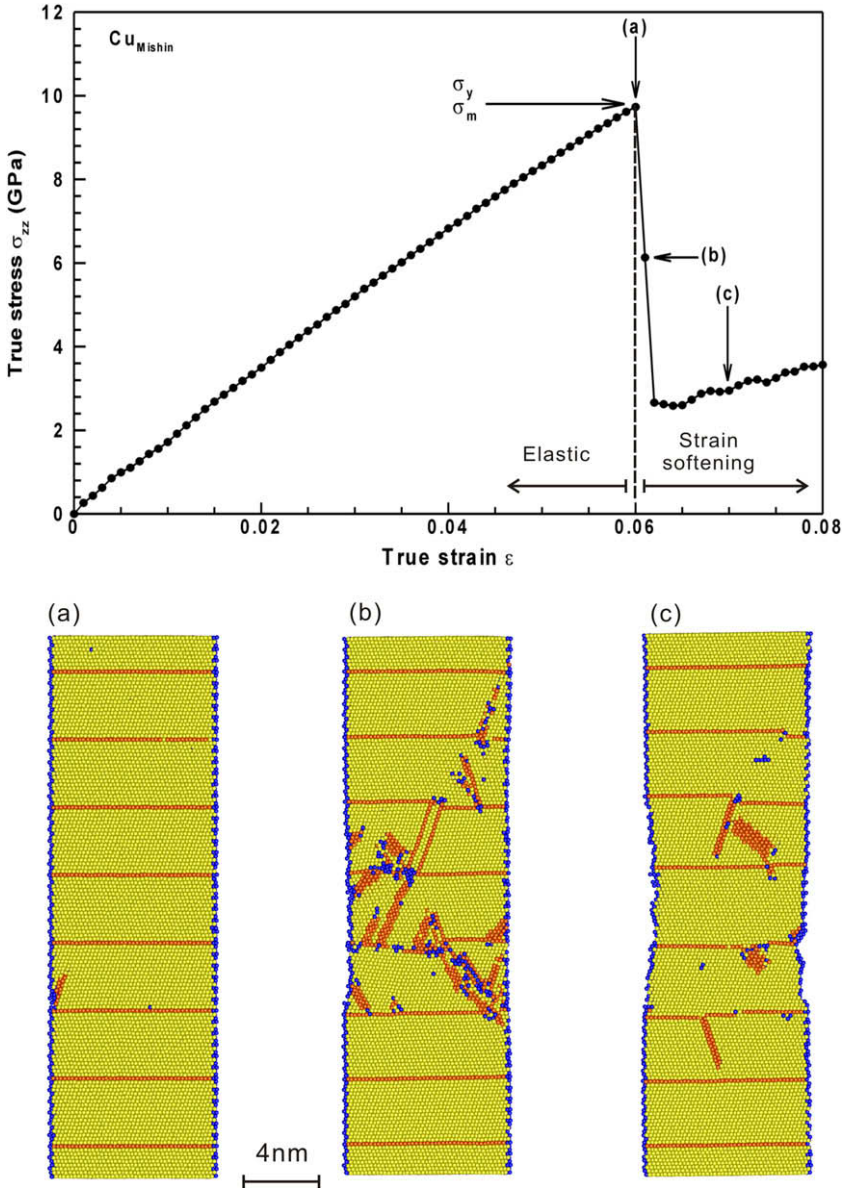

Fig. 4. Tensile stress–strain curve of a twinned Cu nanowire predicted from Mishin EAM potential. Snapshots at different stages of deformation are shown from (a) to (c). (a) Nucleation of the very first partial dislocation at initial yield stress (σ_y). (b) Nanowire deformation after maximum flow stress (σ_m). (c) Escape of previous dislocations at the free surface. Atoms are colored based on the crystal structure.

detailed example of slip transmission at a CTB caused by the nucleation and propagation of a trailing partial from the free surface in the Au_{GRS} NW at a stress near σ_m can be found in the Appendix A.

In Mechanism II, however, it is found that the leading partial dislocations emitted from the surface are directly transmitted through CTBs. This yielding mechanism takes place in metal NWs simulated with Cu_{Mishin}, Ni, Ag_{VC} and Ag_{u3} potentials. A typical example of atomic-scale interactions between a leading partial dislocation and a CTB in the Cu_{Mishin} NW at yield point is represented in Fig. 6b. Here, the leading partial dislocation (γD) from the parent grain directly transmits through the CTB via the reaction:

$$\frac{1}{6}(1\,1\,\bar{1})[\bar{1}\,\bar{1}\,\bar{2}] = \frac{1}{3}(1\,1\,2)[1\,1\,\bar{1}] + \frac{1}{2}(0\,0\,1)[\bar{1}\,\bar{1}\,0]$$

or, using Thompson's notations,

$$\gamma D = \gamma C + CD \quad (1)$$

where $\frac{1}{2}(0\,0\,1)[\bar{1}\,\bar{1}\,0]$ (CD) is a full dislocation transmitted in the twin grain, and $\frac{1}{3}(1\,1\,2)[1\,1\,\bar{1}]$ (γC) represents a sessile stair-rod dislocation remaining in the CTB plane.

Mechanism III, which is associated with deformation twinning, is only observed in the deformation of the Al NW at yield point. In this case, Fig. 6c shows that the first leading partial emitted at yield point is accompanied by the nucleation and propagation of a twinning partial dislocation on a $\{1\,1\,1\}$ plane adjacent to the slip plane of the

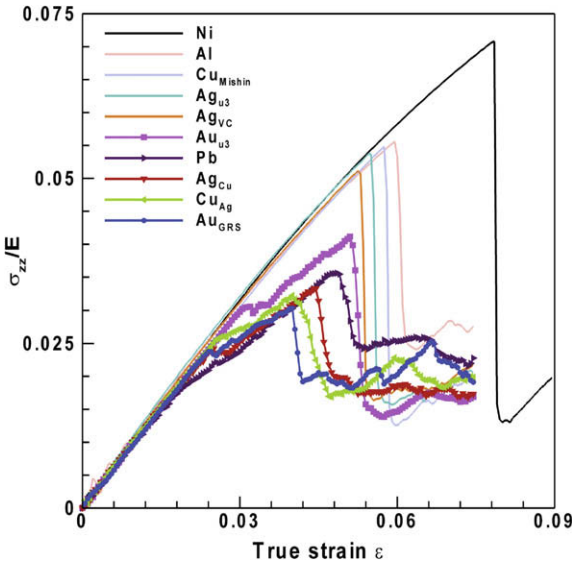

Fig. 5. Tensile stress–strain curves of twinned fcc metal nanowires predicted from different EAM potentials with stress values normalized by the Young's modulus E.

leading partial. Both types of partial dislocation appear to transmit through the CTB according to the same reaction as that described in Eq. (1), except that a twin is left in the parent grain instead of an extended stacking fault. It should be mentioned that similar processes of deformation twinning has been found by Li and Ghoniem [60] to be the dominant mode in nano-twinned Cu films under tensile loading.

4. Discussion

4.1. Dependence of plasticity on γ_{USF} in circular fcc metal NWs with periodic CTBs

Jin et al. [38,39] have pointed out that the lattice resistance for re-nucleating partial dislocations at either a normal glide plane or a common twin plane was related to the unstable stacking fault energy γ_{USF} and unstable twinning energy γ_{UTF}, respectively. Fig. 6 confirms that all slip–twin interactions in twinned fcc metal NWs under tension are dominated by the re-nucleation of dislocation in the twinned grain, instead of the twin plane. Therefore, in the following, we will only refer to γ_{USF} for simplicity. Fig. 7, which represents the relative difference between the tensile yield stress (σ_y) and maximum flow stress (σ_m) for different EAM potentials, shows that the plastic behavior of twinned metal NWs strongly depends upon γ_{USF}. More specifically, a cutoff at $\gamma_{USF} \approx 110$ mJ m^{-2} marks a clear transition from a whisker-like, strain-softening regime to strain-hardening behavior in the plastic deformation of NWs with decreasing values of γ_{USF}. It should be mentioned that in the NW modeled with the Ag_{VC} potential where no hardening occurs, γ_{USF} (=90.4 mJ m^{-2}) is below the cutoff value, which is the only exception. Despite this,

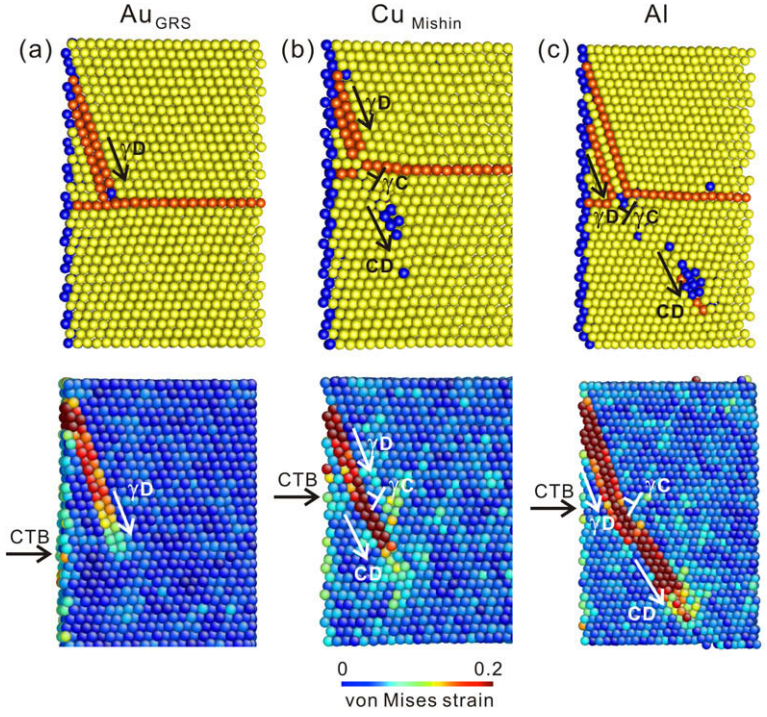

Fig. 6. Snapshots of deformation at atomic-scale in different twinned metal nanowires at initial yield stress (σ_y) in tension. (a) Nucleation of Shockley partial γD and its subsequent blockage by a CTB in an Au nanowire predicted from GRS EAM potential. (b) Transmission of γD through the CTB by reaction $\gamma D = \gamma C + CD$ in Cu nanowire predicted from Mishin EAM potential. (c) Transmission of a twinning partial γD through the CTB by reaction $\gamma D = \gamma C + CD$ in Al nanowire predicted from Mishin EAM potential. Thompson's notations are used next to each dislocation. Atom colors correspond to the crystal structure and local von Mises strain calculations in the upper and lower images, respectively.

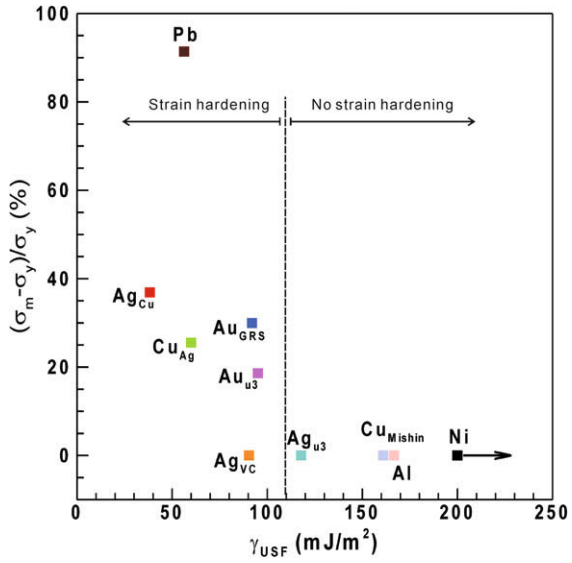

Fig. 7. Relative difference between initial yield stress (σ_y) and maximum flow stress (σ_m) in twinned fcc metal nanowires as a function of the unstable stacking fault energy (γ_{USF}) for different EAM potentials. The γ_{USF} value for Ni has been shifted to the left for clarity.

the Ag NWs predicted from the Ag_{Cu} potential ($\gamma_{USF} = 38.3$ mJ m^{-2}) exhibit a 40% relative increase in stress beyond the limit of elasticity, while this value is as high as 90% in Pb NWs ($\gamma_{USF} = 56.3$ mJ m^{-2}) for the same twin boundary spacing. The values of σ_y, σ_m and γ_{USF} are also listed in Table 1 for comparison.

Another important aspect revealed in Figs. 5 and 7 is that the plasticity of the same metal NW simulated with different EAM potentials can be dramatically different as a function of γ_{USF}. For example, the Ag NW modeled with the EAM potential developed for the Cu–Ag system [47] (Ag_{Cu}, $\gamma_{USF} = 38.26$ mJ m^{-2}) shows significant strain-hardening, as mentioned above, while the NW made of Ag with Foiles' EAM potential [45] (Ag_{u3}, $\gamma_{USF} = 117.86$ mJ m^{-2}) shows no strain-hardening at all. Similar conclusions can be drawn for the deformation of Cu NWs predicted from the potential for the Cu–Ag system (Cu_{Ag}, $\gamma_{USF} = 60.0$ mJ m^{-2}) [47] and Mishin's EAM potential (Cu_{Mishin}, $\gamma_{USF} = 161.0$ mJ m^{-2}) [48].

4.2. Maximum CTB resistance against dislocation glide and its comparison to dislocation nucleation stress

We can conclude from Figs. 3–6 and Table 1 that strain-hardening effects only occur when the CTBs are able to block the leading partial dislocations emitted from the free surface at the initial yield point, which corresponds to the yielding mechanism I. To gain predictive understanding of yielding mechanisms in fcc metal NWs in tension, it is therefore important to quantitatively assess the maximum stress, σ_R, for the resistance of CTBs to the glide of partial dislocations, regardless of surface effects. For that purpose, we have simulated the tensile behavior of a fully periodic model with no free surfaces containing two pure edge partial dislocations that are forced to intersect two CTBs as shown in Fig. 2. The procedure to determine σ_R from this model is described in Section 2.2. Under tensile loading, the two $\{1\,1\,1\}\langle 1\,1\,2\rangle$ partial dislocations move in opposite directions and are blocked by the CTBs at the early stage of deformation. During this process, the flow stress linearly increases with the applied strain until the stress drops after one of the partial dislocations overcomes the slip resistance imposed by the CTBs. A caveat in this model is that the partial dislocations emitted from the surface of twinned metal NWs are semi-circular loops, which present both screw and edge components. However, our analysis of Mechanisms I–III in Fig. 6a–c has shown that the screw component of the partial dislocations in twinned NWs has no significant effect on the transmission of the dislocation through the CTB. Therefore, our cubic model should also provide meaningful results about the maximum CTB resistance σ_R against dislocation glide in fcc metal NWs.

We now aim to compare σ_R to the stress required to emit new dislocations. To this end, Fig. 8a includes the dislocation nucleation stresses in twin-free bulk metals (σ_{HN}), twin-free circular metal NWs (σ_{SC}) and twinned circular metal NWs (σ_y) under tension. The values of σ_{HN}, σ_{SC} and σ_y are also listed in Table 1 for comparison. Fig. 8a and b show that σ_y, σ_{SC}, σ_{HN} and σ_R linearly increase with γ_{USF}. As indicated by the trend lines in Fig. 8a, the stress required for surface-assisted dislocation nucleation in twinned (σ_y) and twin-free NWs (σ_{SC}) are close for this particular NW geometry. However, we should emphasize that both stresses are significantly smaller than that in twin-free metals with no free surfaces (σ_{HN}); the latter being characterized by homogeneous dislocation nucleation. Furthermore, the trend lines in Fig. 8b representing the evolution of σ_y and σ_R as a function of γ_{USF} intersect each other at $\gamma_{USF} \approx 115$ mJ m^{-2}, which is very close to the cutoff value shown in Fig. 7 (110 mJ m^{-2}). This result strongly supports the idea that the transition in plasticity from strain-softening to strain-hardening in twinned metal NWs is correlated with the influence of unstable stacking fault energy when the surface-assisted nucleation stress (σ_y) becomes larger than the maximum CTB resistance against the glide of partial dislocations (σ_R).

4.3. Linear dependence of surface dislocation nucleation on γ_{USF}

The analysis by Rice [40] has shown that γ_{USF} plays an important role in determining the critical condition for the emission of a partial dislocation at a crack tip. Asaro and Suresh [61] extended Rice's model by using γ_{USF} as a parameter for the nucleation of partial dislocations from sources in grain boundaries, where higher local stresses can be encountered. We also found that in twinned Au NWs under tension, the dislocation nucleation process occurred at specific sites corresponding to the intersection of CTBs with the free surface, which acted as stress concen-

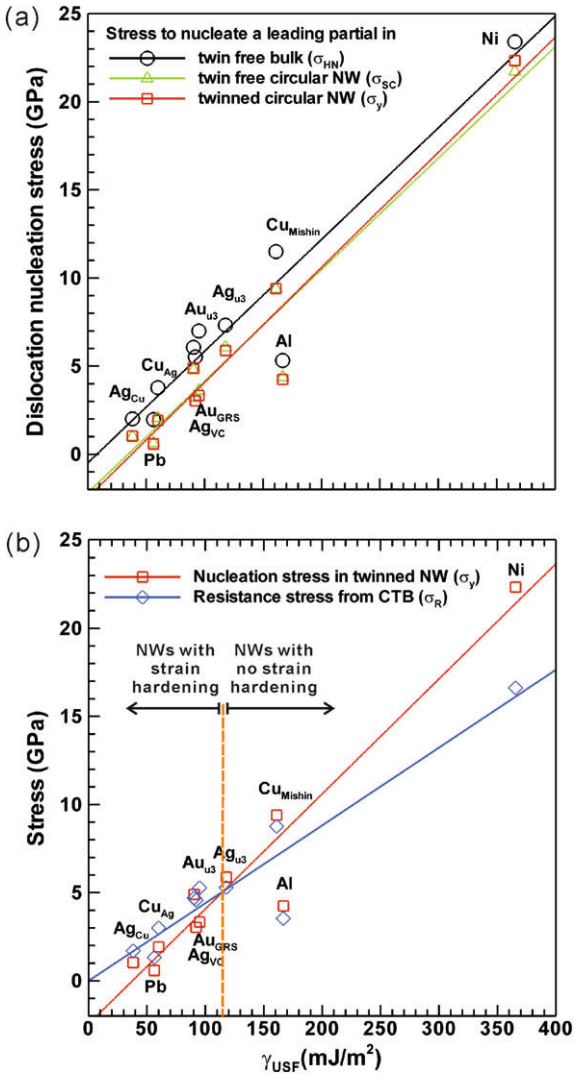

Fig. 8. Dependence of plastic behavior on the unstable stacking fault energy (γ_{USF}) in fcc metals. (a) Required stress for dislocation nucleation in twin-free cubic bulk (σ_{HN}), twin-free circular nanowire (σ_{SC}), twinned circular nanowire (σ_y), and (b) the maximum stress for the resistance of CTBs to the glide of partial dislocations (σ_R) as a function of γ_{USF}.

trations [62]. As such, the parameter γ_{USF} should also play a critical role in the emission of new partials from the surface of twinned fcc metal NWs. Based on Rice's analysis, we can therefore derive an equation to characterize the emission of $\{1\,1\,1\}\langle 1\,1\,2\rangle$ leading partial dislocations in twinned NWs as follows:

$$\int_0^{b_p/2} \tau(x)dx = \gamma_{USF} \tag{2}$$

where $\tau(x)$ is the shear stress required to displace the lattice by a distance x along the $\{1\,1\,1\}\langle 1\,1\,2\rangle$ slip direction and b_p is the magnitude of the partial Burgers vector ($b_p = a/\sqrt{6}$). As suggested in Ref. [40], the stress $\tau(x)$ increases approximately linearly from 0 at $x = 0$ to a maximum τ_{max} and decreases again linearly to 0 at $x = b_p/2$. Integrating the left-hand side of Eq. (2) with this approximation yields:

$$\frac{1}{2}\cdot\tau_{max}\cdot\frac{b_p}{2} = \gamma_{USF} \tag{3}$$

with

$$\tau_{max} = \tau_{appl} - \tau_0 \tag{4}$$

where τ_0 is an image stress imposed by both free surface and CTBs on the dislocation glide [32], which is only affected by the NW geometry and should be identical for all metal NWs studied, τ_{appl} is the resolved shear stress due to the applied axial deformation. Based on Schmid's law,

$$\tau_{appl} = m\cdot\sigma_y \tag{5}$$

where m is the Schmid factor with $m = 0.31$ for a $\langle 1\,1\,2\rangle$-type partial dislocation. Combining Eqs. (2)–(5) yields:

$$\sigma_y = \frac{4\gamma_{USF}}{0.31b_p} + \frac{\tau_0}{0.31} \tag{6}$$

Eq. (6) indicates that the yield stress σ_y is proportional to γ_{USF} with a linear dependence of slope $\frac{4}{0.31b_p} \approx 7.8\times 10^{10}/m$, which is close to the slope of the trend line for σ_y in Fig. 8b ($6.5\times 10^{10}/m$). Within the limits of our approximation, the theoretical prediction from Eq. (6) therefore appears to be in excellent agreement with the simulation results. Similarly, the resistance stress from CTBs σ_R in our study can be characterized as the lattice resistance for nucleating new dislocations at a normal glide plane from the CTB based on the analysis by Jin et al. [38–39]. Therefore σ_R should also vary linearly as a function of γ_{USF}.

4.4. Application of atomistic predictions to realistic NWs

The relevance of our atomistic predictions to realistic NWs can be assessed by asking three fundamental questions. First, are periodically twinned microstructures realistically linked to fcc metal NWs? Second, can the mechanism of plasticity predicted from simulation be altered by the NW geometry, e.g. if the NW surface is faceted instead of perfectly circular? Third, does the accuracy in determining the generalized stacking fault energy curve with different potentials influence the plasticity of twinned NWs?

4.4.1. Microstructures

Periodically distributed (1 1 1) CTBs have been synthesized in the microstructure of semiconducting NWs [63–67], as well as Au and Cu NWs with [1 1 1] orientation [25]. However, other types of twin boundary have also been formed by controlling the deposition conditions. For example, lengthwise $(1\,1\,1)[1\,1\,\bar{2}]$ twins in $[1\,1\,\bar{2}]$ oriented Cu NW [25] and fivefold twinning structures in [0 1 1]-oriented Ag NWs [3] have been observed. It is worth noting that the yield strength of the Ag NWs appears to be substantially reduced after thermal annealing to eliminate the fivefold twin structure [3]. This effect confirms that fivefold twin boundaries can significantly harden the Ag NW, which is consistent with our atomistic predictions. It should be noted however that in realistic NWs, other types of defect such as atomic ledges can exist in CTBs, which sig-

nificantly affect the strength and deformation of the material. For example, Lu et al. [68] have found that in nanotwinned Cu, a shift in yielding mechanism can occur from slip transfer across CTBs to easy dislocation nucleation from pre-existing atomic ledges at twin planes when the interspacing between CTBs were reduced below a critical value. Also, the geometry of fivefold twinned Ag NWs is pentagonal, as opposed to circular, which is likely to contribute in decreasing the stress for dislocation nucleation, and therefore increasing the strain-hardening regime, as shown below.

4.4.2. NW geometry

A key feature of this MD investigation is that the transition of plasticity from strain-softening to strain-hardening in twinned metal NWs under tension can be varied by changing the sample geometry, as proposed by Zhang and Huang [30,31]. While the penetration stress σ_R is related to the intrinsic resistance to slip in the metal and should not vary significantly with change in sample shape, the dislocation nucleation stress σ_y has been found to be highly dependent on the geometry [18,30,31]. It is revealed from Fig. 8a that the free surface decreases the dislocation nucleation stress in NWs. Similarly, Zhang and Huang [30,31] have shown that a twinned Cu NW requires a lower stress to nucleate dislocations with a square cross-section than a circular cross-section. Therefore, it is possible to enable strain-hardening in metal NWs that show no initial strain-hardening when circular, by modifying the geometry of the NW cross-section in order to decrease σ_y without altering σ_R. To support this idea, we simulated the tensile behavior of twinned Ag NWs with both circular and square cross-sections using Foiles' EAM potential [45]. It was found in Figs. 5, 7 and 8b that no strain-hardening occurs in twinned Ag NWs with circular cross-section, using this potential. However, the tensile stress–strain curves in Fig. 9 clearly

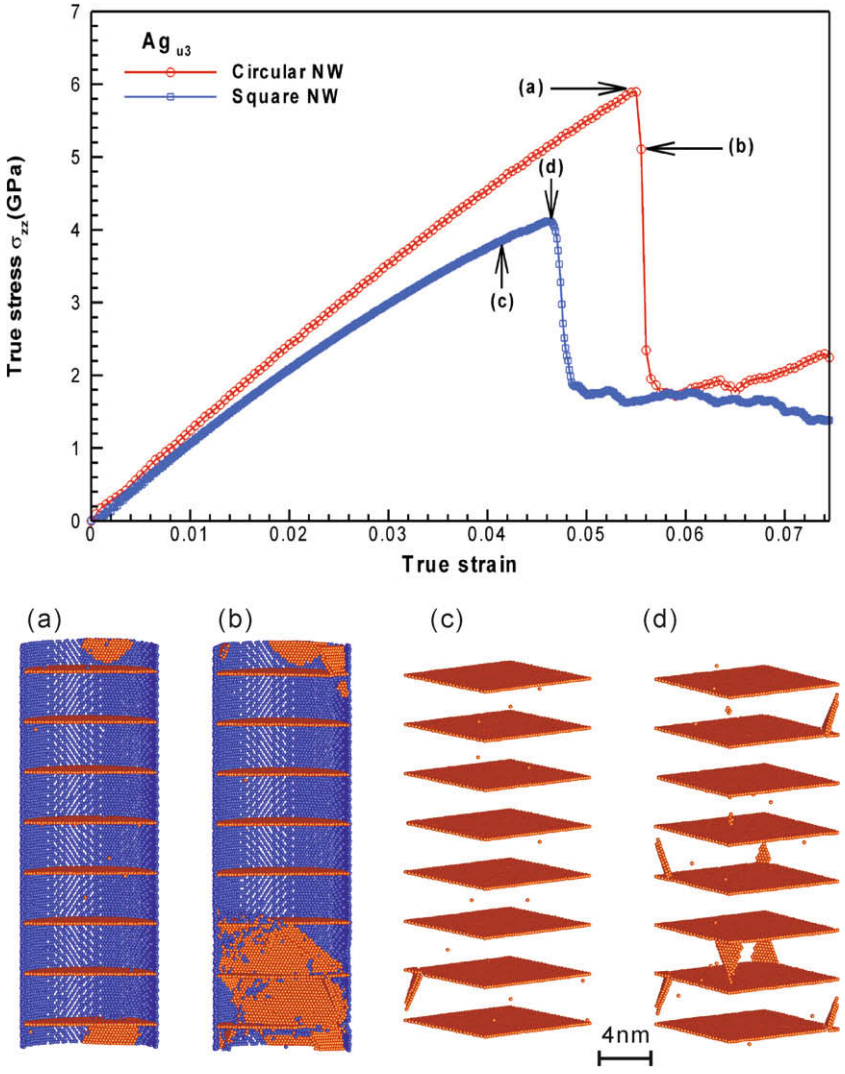

Fig. 9. Tensile stress–strain curves of twinned Ag nanowires with either circular or square cross-section predicted from FBD's EAM potential. Snapshots at different stages of deformation are shown from (a) to (d). Nucleation of the very first partial dislocation in (a) circular and (c) square cross-section NW. (b) Circular nanowire past the maximum flow stress. (d) Square nanowire at maximum flow stress. Atom colors correspond to the crystal structure. Perfect fcc atoms and the nanowire front in (a) and (b) as well as free surface atoms in (c) and (d) have been removed for clarity.

show that in the square Ag NW, significant strain-hardening is enabled as the stress continues to increase after the yield point. The atomistic model in Fig. 9d also confirmed that the nucleated partial dislocations were blocked by the CTBs after the initial yield point in the square Ag NW, which provides further evidence for Mechanism I.

4.4.3. Interatomic potential

Another interesting aspect of our study is that the same type of metal NW behaves differently under tension when predicted from different EAM potentials (Fig. 5). Specifically, we found some large variations in the unstable stacking fault energy for both Cu and Ag, as a function of the interatomic potential, which causes either strain-hardening or strain-softening during the plastic deformation of the Cu and Ag NWs (see Table 1). Moreover, Pb NW predicted from the EAM potential for Pb–Cu alloy shows the maximum hardening with a 90% relative increase of flow stress after the yield point. A caveat is that these atomistic predictions can only be relevant to realistic NWs if the EAM potentials used can faithfully model the generalized stacking fault energy curve of the metal, in comparison to data from either experiments or first-principles calculations. As for dislocation nucleation and interaction [42], the intrinsic stacking fault energy γ_{SF} should be used as a criterion to evaluate the accuracy of the EAM potentials. For example, Table 1 shows that the γ_{SF} value of Au is in better agreement with experimental data when predicted from the GRS potential than Foiles' potential. Similarly, the VC potential best predicts the γ_{SF} values for pure Ag and those from Mishin's EAM potentials for Cu, Al and Ni are all consistent with the reference values.

5. Conclusions

The tensile deformation of fcc metal NWs containing periodically distributed (1 1 1) CTBs has been addressed by MD simulations using 10 different EAM interatomic potentials. The major conclusions drawn from this investigation are twofold. First, a fundamental transition of plasticity in twinned metal NWs from sharp yield and strain-softening to significant strain-hardening occurs when the unstable stacking fault energy γ_{USF} of the metal decreases. Our findings may therefore resolve some conflicting observations made in the past, since not all fcc metal NWs possess the same behavior. Second, strain-hardening is enabled in NWs when the stress for dislocation emission from the free surface becomes smaller than the maximum stress for the resistance of CTBs to dislocation glide, with both stresses proportional to γ_{USF}. The specific mode of plastic deformation predicted in fcc metal NWs with nanoscale twins also appears to depend on the NW geometry and the potential accuracy in determining the generalized planar and stacking fault energy curves. This investigation therefore provides further fundamental understanding on twin boundary effects in metal plasticity within constrained dimensions.

Acknowledgements

Support from NSF CAREER program (Grant DMR-0747658) and the computational resources by the Vermont Advanced Computing Center (Grant NASA NNX06AC88G) are gratefully acknowledged.

Appendix A

Snapshots of the cross-slip pathway at the intersection of dislocations with CTBs in the Au NW are shown in Fig. A1, with atom colors corresponding to the crystal structure [51] and local von Mises strain calculations [58,59] in the upper and lower images, respectively. Fig. A1a shows that a trailing partial ($B\gamma$) is emitted from the free surface, and recombines with the leading partial (γD) originally blocked by a CTB at the initial yield point, in order to form a full $\langle 1\,1\,0\rangle$ dislocation (BD) via the reaction:

$$\frac{1}{6}(1\,1\,\bar{1})[1\,\bar{2}\,\bar{1}] + \frac{1}{6}(1\,1\,\bar{1})[\bar{1}\,\bar{1}\,2] = \frac{1}{2}(1\,1\,\bar{1})[0\,\bar{1}\,\bar{1}]$$

or, using Thompson's notations,

$$B\gamma + \gamma D = BD \tag{A.1}$$

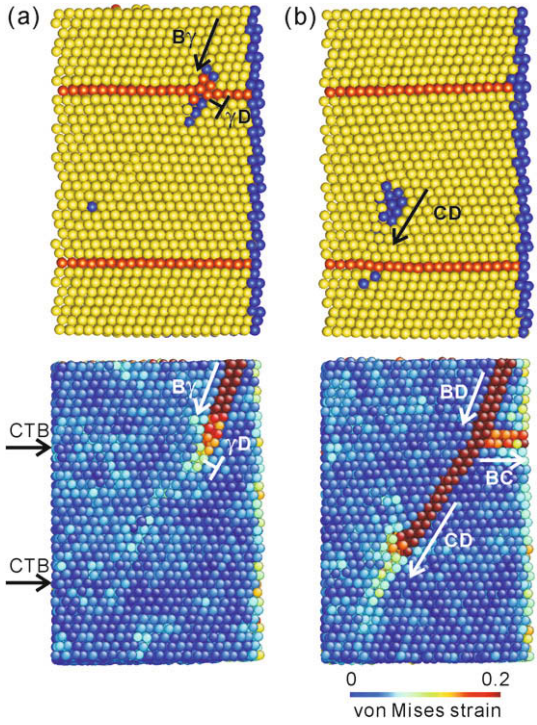

Fig. A1. Snapshots of deformation at atomic-scale in a periodically twinned Au nanowire at the maximum flow stress (σ_m) predicted from GRS EAM potential. (a) Emission of a trailing partial dislocation ($B\gamma$) and formation of a full dislocation (BD) via the reaction $B\gamma + \gamma D = BD$. (b) Transmission of the full dislocation through the CTB by the reaction, 8.5 ps later. Thompson's notations are used next to each dislocation. Atom colors correspond to the crystal structure and local von Mises strain calculations in the upper and lower images, respectively.

The full dislocation $\frac{1}{2}(1\,1\,\bar{1})[0\,\bar{1}\,\bar{1}]$ (BD) then transmits to the twin grain (Fig. A1b) by the reaction:

$$\frac{1}{2}(1\,1\,\bar{1})[0\,\bar{1}\,\bar{1}] = \frac{1}{2}(1\,1\,1)[1\,0\,\bar{1}] + \frac{1}{2}(0\,0\,1)[\bar{1}\,\bar{1}\,0]$$

or

$$BD = BC + CD \tag{A.2}$$

where $\frac{1}{2}(0\,0\,1)[\bar{1}\,\bar{1}\,0]$ (CD) is the full dislocation transmitted in the twin grain, and $\frac{1}{2}(1\,1\,1)[1\,0\,\bar{1}]$ (BC) is a full dislocation gliding on the twin plane.

References

[1] Wu B, Heidelberg A, Boland JJ. Nat Mater 2005;4:525.
[2] Greer JR, Nix WD. Appl Phys A 2005;80:1625.
[3] Wu B, Heidelberg A, Boland JJ. Nano Lett 2006;6:468.
[4] Greer JR, Nix WD. Phys Rev B 2006;73:245410.
[5] Volkert CA, Lilleodden ET. Philos Mag 2006;86:5567.
[6] Shan ZW, Mishra RK, Asif SAS, Warren OL, Minor AM. Nat Mater 2008;7:115.
[7] Kim JY, Greer JR. Appl Phys Lett 2008;93:101916.
[8] Frick CP, Clark BG, Orso S, Schneider AS, Arzt E. Mater Sci Eng A 2008;489:319.
[9] Oh SH, Legros M, Kiener D, Dehm G. Nat Mater 2009;8:95.
[10] Buzzi S, Dietiker M, Kunze K, Spolenak R, Löffler JF. Philos Mag 2009;89:869.
[11] Diao J, Gall K, Dunn ML. Nano Lett 2004;4:1863.
[12] Gall K, Diao J, Dunn ML. Nano Lett 2004;4:2431.
[13] Hyde B, Espinosa HD, Farkas D. JOM 2005;57:62.
[14] Park HS, Zimmerman JA. Phys Rev B 2005;72:054106.
[15] Diao J, Gall K, Dunn ML, Zimmerman JA. Acta Mater 2006;54:643.
[16] Rabkin E, Srolovitz DJ. Nano Lett 2007;7:101.
[17] Ji C, Park HS. Nanotechnology 2007;18:305704.
[18] Cao A, Ma E. Acta Mater 2008;56:4816.
[19] Pastor-Abia L, Caturla MJ, SanFabián E, Chiappe G, Louis L. Phys Rev B 2008;78:153410.
[20] Li X, Yang W. J Nanomater 2009;2009:245941.
[21] Seeger A. In: Fisher JC, Johnston WG, Thomson R, editors. Dislocations and mechanical properties of crystals. New York: John Wiley; 1957. p. 243–329.
[22] Brenner SS. J Appl Phys 1959;30:266.
[23] Monk J, Farkas D. Philos Mag 2007;87:2233.
[24] Maaβ R, Petegem SV, Zimmermann J, Borca CN, Swygenhoven HV. Scripta Mater 2008;59:471.
[25] Tian M, Wang J, Kurtz J, Mallouk TE, Chan MHW. Nano Lett 2003;3:919.
[26] Wang J, Tian M, Mallouk TE, Chan MHW. J Phys Chem B 2004;108:841.
[27] Afanasyev KA, Sansoz F. Nano Lett 2007;7:2056.
[28] Deng C, Sansoz F. Nano Lett 2009;9:1517.
[29] Cao AJ, Wei YG, Mao SX. Appl Phys Lett 2007;90:151909.
[30] Zhang Y, Huang H. Nanoscale Res Lett 2009;4:34.
[31] Zhang Y, Huang H, Atluri SN. CMES 2008;35:215.
[32] Chen Z, Jin Z, Gao H. Phys Rev B 2007;75:212104.
[33] Yamakov V, Wolf D, Phillpot SR, Gleiter H. Acta Mater 2003;51:4135.
[34] Zhu T, Li J, Samanta A, Kim HG, Suresh S. Proc Nat Acad Sci 2007;104:3031.
[35] Asaro RJ, Kulkarni Y. Scripta Mater 2008;58:389.
[36] Tsuru T, Shibutani Y, Kaji Y. Phys Rev B 2009;79:012104.
[37] Lu L, Dao M, Zhu T, Li J. Scripta Mater 2009;60:1062.
[38] Jin ZH, Gumbsch P, Albe K, Ma E, Lu K, Gleiter H, et al. Acta Mater 2008;56:1126.
[39] Jin ZH, Gumbsch P, Ma E, Albe K, Lu K, Hahn H, et al. Scripta Mater 2006;54:1163.
[40] Rice JR. J Mech Phys Solids 1992;40:239.
[41] Bernstein N, Tadmor EB. Phys Rev B 2004;69:094116.
[42] Zimmerman JA, Gao H, Abraham FF. Model Simul Mater Sci Eng 2000;8:103.
[43] Plimpton SJ. J Comp Phys 1995; 117: 1. <http://lammps.sandia.gov>.
[44] Grochola G, Russo SP, Snook IK. J Chem Phys 2005;123:204719.
[45] Foiles SM, Baskes MI, Daw MS. Phys Rev B 1986;33:8983.
[46] Voter AF, Chen SP. Mat Res Soc Symp Proc 1987;82:175.
[47] Williams PL, Mishin Y, Hamilton JC. Model Simul Mater Sci Eng 2006;14:817.
[48] Mishin Y, Mehl MJ, Papaconstantopoulos DA, Voter AF, Kress JD. Phys Rev B 2001;63:224106.
[49] Mishin Y, Farkas D, Mehl MJ, Papaconstantopoulos DA. Phys Rev B 1999;59:3393.
[50] Hoyt JJ, Garvin JW, Webb III EB, Asta M. Model Simul Mater Sci Eng 2003;11:287.
[51] Ackland GJ, Jones AP. Phys Rev B 2006;73:054104.
[52] Hirth JP, Lothe J. Theory of dislocations. 2nd ed. New York: Wiley; 1982.
[53] Carter CB, Ray ILF. Philos Mag 1977;35:189.
[54] Rautioaho RH. Phys Status Solidi B 1982;112:83.
[55] Westmacott KH, Peck RL. Philos Mag 1971;23:611.
[56] Bailey JA, Singer ARE. J Inst Metals 1963;92:404.
[57] Balluffi RW. J Nucl Mater 1978;69 & 70:240.
[58] Shimizu F, Ogata S, Li J. Mater Trans 2007;48:2923.
[59] Li J. Model Simul Mater Sci Eng 2003;11:173.
[60] L L, Ghoniem NM. Phys Rev B 2009;79:075444.
[61] Asaro RJ, Suresh S. Acta Mater 2005;53:3369.
[62] Deng C, Sansoz F. Appl Phys Lett 2009;95:091914.
[63] Banerjee R, Bhattacharya A, Genc A, Arora BM. Philos Mag Lett 2006;86:807.
[64] Arbiol J, Morral AFI, Estrade S, Peiro F, Kalache B, Cabarrocas PRI, et al. J Appl Phys 2008;104:064312.
[65] Wang DH, Xu D, Wang Q, Hao YJ, Jin GQ, Guo XY, et al. Nanotechnology 2008;19:215602.
[66] Shim HW, Zhang Y, Huang H. J Appl Phys 2008;104:063511.
[67] Algra RE, Verheijen MA, Borgström MT, Feiner LF, Immink G, Enckevort WJPV, et al. Nature 2008;456:369.
[68] Lu L, Chen X, Huang X, Lu K. Science 2009;323:607–10.